Available online at www.sciencedirect.com
SCIENCE DIRECT®

Journal of the European Ceramic Society 24 (2004) 2247–2258
www.elsevier.com/locate/jeurceramsoc

Modified thick thermal barrier coatings: Microstructural characterization

S. Ahmaniemi[a,*], M. Vippola[a], P. Vuoristo[a], T. Mäntylä[a], F. Cernuschi[b], L. Lutterotti[c]

[a]*Tampere University of Technology, Institute of Materials Science, PO Box 589, 33101 Tampere, Finland*
[b]*CESI, Via Reggio Emilia, 39, 20090 Segrate, Italy*
[c]*Universita Degli Studi di Trento, Ingegneria dei Materiali, Via Mesiano 77, 38050 Trento, Italy*

Received 6 March 2003; received in revised form 19 June 2003; accepted 6 July 2003

Abstract

Thick thermal barrier coatings were modified with laser glazing and phosphate based sealing treatments. Surface porosity of the sealed coatings decreased significantly in all cases. Structural analysis showed a strong preferred crystal orientation of the t′ZrO_2 phase in direction [002] in laser-glazed 25CeO_2–2.5Y_2O_3–ZrO_2 coating. In laser-glazed 22MgO–ZrO_2 coating the major phase was rhombohedral $Mg_2Zr_5O_{12}$. In phosphate sealed 8Y_2O_3–ZrO_2 coating the strengthening mechanism was identified as adhesive binding without chemical bonding. Coating microstructures were determined by scanning electron microscopy, energy dispersive spectroscopy, transmission electron microscopy and optical microscopy. Coatings were also characterized by X-ray diffraction, microhardness and porosity.

Keywords: Functional applications; Microstructural characterization; TBC; Thermal barrier coatings; ZrO_2

1. Introduction

Plasma sprayed zirconia coatings are widely used as thermal barrier coatings (TBC) in gas turbine hot section components such as burners, transition ducts, vanes and blades. Instead their use in diesel engine combustion chamber components has been quite rare, because of the long run durability problems in such conditions. For that reason, there have been many investigations in developing proper TBCs for diesel engines.[1–7] The conditions in diesel engine combustion chambers differ considerably from those of gas turbine hot sections. In diesel engines the mean temperature levels of TBC surfaces are much lower than in gas turbines, but the number of thermal cycles and shocks are correspondingly higher. The varying pressure within the diesel engine cycle causes severe mechanical loads and stresses to the surfaces of the combustion chamber component that are not comparable to conditions of gas turbines. Low and medium speed diesel engines in marine and energy production applications use normally variable grades of liquid fuels that contain impurities such as S, V and Na. Because of the high amount of impurities and quite low mean temperature in the combustion chamber of diesel engines, the conditions are favorable for hot corrosion. For these reasons the major failure mechanisms that cause TBC spallation in diesel engines are hot corrosion, thermal cycling and mechanical loading while in gas turbine more presumable coating failure is caused by coating-substrate interface stresses induced by bond coat oxidation.[8,9]

Increasing the turbine hot gas inlet temperature (TIT) is a potential way to improve the efficiency of the gas turbine driven combined cycle process. At the moment in land based gas turbines the maximum TIT is around 1500 °C and in aero engines even higher. Since the structural materials, nickel and cobalt based superalloys, can not face temperatures higher than 950 °C, TBCs with better insulation properties are needed. With thicker TBCs the mean combustion temperature of the diesel process can also be increased. The increased temperature does not affect directly the efficiency of the diesel process, but this extra heat can be recovered in a

* Corresponding author. Present address: Metso Paper Inc., Global Service Operations PO Box 587, 40101 Jyväskylä, Finland. Tel.: +358-20-482-6837.
E-mail address: samppa.ahmaniemi@metso.com (S. Ahmaniemi).

0955-2219/$ - see front matter © 2003 Elsevier Ltd. All rights reserved.
doi:10.1016/S0955-2219(03)00639-3

turbocharger or in a flue gas boiler in combined cycle. Some studies have also shown that TBCs lower the fuel consumption of the diesel process.[1,7]

At the moment in most applications the thickness of TBCs is below 500 μm, because of their limited reliability. Normally the increased thickness of TBCs leads to a reduced coating lifetime. Normally we can say that the thicker the coating—the higher the temperature gradient through the coating—the higher the stresses in the coating. Even if the coefficient of thermal expansion (CTE) of $8Y_2O_3$–ZrO_2 is close to that of the substrate material, the CTE difference of the substrate and coating induces stresses at high temperatures at the coating interface. The strain tolerance of TTBC has to be managed by controlling the coating microstructure.

Use of thicker coatings generally leads to the higher coating surface temperatures that can be detrimental, if a certain limit is exceeded. In the long run, the phase structure of yttria stabilized zirconia $8Y_2O_3$–ZrO_2 is not stable above the 1250 °C and can be unstabilized quite fast at 1400 °C.[10] Also the strain tolerance of the coating can be reduced rapidly by sintering effects, if too high surface temperatures are allowed.[11] For these reasons several cooling techniques of the gas turbine component are used to control the surface temperatures of the TBCs.

There have been several attempts to enhance the properties of the plasma sprayed TTBCs by various sealing and modification processes. Sealing treatments have been used mainly for improving the hot corrosion properties and erosion resistance of the coatings by closing the open pores on the coating surface. The modification of the open porosity in TBCs has been approached by liquid metal impregnation,[12] laser-glazing,[13–17] hybrid spray processing[18] solar furnace heat treatment,[19] hot isostatic pressing (HIP) [20,21] sol-gel processing,[22–24] phosphate impregnation,[25–27] or by thin CVD overlay coatings.[28] Organic sealants are mainly used for corrosion protection at lower temperatures.[29] The other modification processes are mainly focused to increase the strain tolerance of TTBCs by lowering the stiffness of the coating. Lots of studies have been related to reducing Young's modulus and residual stresses of the thick TBCs.[30–33] In practice these can be achieved by controlling the spray parameters, but also controlling the substrate and coating temperature during the coating deposition. If the system heats too much in spraying, compressive stresses are formed into the ceramic coating. For that reason active substrate and surface cooling is normally used during spraying. Spray parameters can also be fixed to obtain desired level of porosity and microcracks. Vertical segmentation cracks, which can go through the whole coating, can be produced by introducing rather thick spray passes in coating deposition.[30] Segmentation cracks are very effective in lowering the Young's modulus of the TTBCs. For that reason they can increase the lifetime of the coating in thermal cycling significantly.[31] In addition to strain tolerance, pores and especially the horizontal cracks are naturally advantageous in lowering the thermal conductivity of the coating. Extremely high porosity values (up to 25 vol.%) of TBCs have been obtained by spraying polymers together with zirconia.[32] However, when spraying very porous and thick coatings the deposition efficiency (DE) decreases, but also mechanical properties, such as erosion resistance, decreases. When modifying the TBC structures one should remember that the coating primary functions, such as thermal insulation and strain tolerance, should not be deteriorated.

In this study the microstructures of modified $8Y_2O_3$–ZrO_2, $25CeO_2$–$2.5Y_2O_3$–ZrO_2 and $22MgO$–ZrO_2 TTBCs were characterized. The goal was to find a method to produce a dense top layer to TTBC with possibly better mechanical properties and hot corrosion resistance. On the other hand we tried to tailor the vertical crack network by laser-glazing in order to seek a microstructure for better strain tolerance. In this paper we introduce laser-glazing and phosphate based sealing treatment procedures, characterize the modified coating structures and discuss their respective structural advantages and drawbacks.

2. Experimental

2.1. Sample preparation

Coatings were air plasma sprayed with plasma spray equipment (Plasma-Technik A3000S, Sulzer Metco AG, Wohlen, Switzerland) using the spray parameters presented in Table 1. $8Y_2O_3$–ZrO_2 and $25CeO_2$–$2.5Y_2O_3$–ZrO_2 powders were from Sulzer Metco (Wohlen, Switzerland) and $22.5MgO$–ZrO_2 powder from Praxair (Indianapolis, IN, USA). Coatings were sprayed on the cleaned and grit blasted AISI4142 steel substrates ($Ø = 25$ mm, $h = 5$). Surface roughness (R_a) after the grit blasting (corundum, 40 grit) was at the range of 6–7 μm. Substrate temperature was measured during the spraying and it was kept below 200 °C by pressurized air-cooling. Targeted coating thickness was 1000 μm. Free-standing coating specimens for mercury porosimetry (MP) studies were etched from substrates using $50HCl/50H_2O$ solution.

2.2. Laser glazing

Coatings were laser-glazed using a 4 kW continuous wave fiber coupled HAAS HL4006D lamp-pumped Nd-YAG laser (HAAS-laser GmbH, Schramberg, Germany). In the glazing experiments the laser was equipped with an integrated water-cooled copper mirror with an effective focal length of 100 mm. The width of the laser

Table 1
Plasma spray parameters and coating abbreviations

	$8Y_2O_3$–ZrO_2	$25CeO_2$–$2.5Y_2O_3$–ZrO_2	22.5MgO–ZrO_2
Coating abbreviation	8Y	25C	22M
Trade name	Metco 204 NS	Metco 205 NS	Praxair ZRO 103
Powder type	HOSP[a]	HOSP	F/C[b]
Particle size (μm)	−125 + 11	−90 + 16	−75 + 10
Current (A)	600	600	600
Voltage (U)	71.0	70.0	70.3
Argon flow rate (l/min)	35	35	35
Hydrogen flow rate (l/min)	12	12	12
Carrier gas (Ar) flow rate (l/min)	2.6	2.6	2.4
Injector Ø (mm)	1.8	1.8	1.8
Injector angle (°)	90	90	90
Axial powder feed distance (mm)	6	6	6

[a] HOSP = hollow spherical powder.
[b] F/C = fused and crushed powder.

beam was 10 mm at the focused area, which was at the distance of 80 mm from the mirror. Three parallel 10 mm wide tracks, with 2 mm overlapping, were used to glaze the whole specimen surface. Before the final preparation of the studied coatings, laser glazing parameters were optimized by comparing coating microstructures with different specific laser energy densities using continuous and pulsed laser beams. In the optimization stage of the laser glazing the predetermined melting depth of the coating surface was reached, without causing coating spallation. Also formation of too long vertical cracks, which pass through the thickness of the coating, was avoided. Laser glazing parameters and coating abbreviations are presented in Table 2.

2.3. Aluminum phosphate impregnation

8Y and 25C coatings were sealed with $Al(OH)_3$–$(85\%)H_3PO_4$ solution diluted with 20 wt.% of deionized water. The ratio of $Al(OH)_3$:$(85\%)H_3PO_4$ was 1:4.2 by weight which corresponds to the molar ratio P/Al of about 3. The solution was mixed and slightly heated with magnetic stirrer until it became clear. The 22M coating was sealed with orthophosphoric acid $(85\%)H_3PO_4$. The sealant was spread on to the surface just before the heat treatment. The free standing coatings for mercury porosimetry studies were sealed from both sides after the etching. Heat treatment was performed at 300 °C for 4 h. The names of the aluminum phosphate sealed 8Y and 25C coatings were abbreviated as 8YAP and 25CAP, respectively and orthophosphoric acid sealed 22M coating as 22MOPA.

2.4. Characterization

Polished microsections and fracture planes were prepared for microscopy analysis. The coating microstructure was determined by optical microscopy (Leitz, Wetzlar, Germany), scanning electron microscopy (SEM, Model XL-30, Philips, Eindhoven, Netherlands) and transmission electron microscopy (TEM, Model JEM 2010, Jeol, Tokyo, Japan). In TEM studies selected area electron diffraction (SAED) was used to study the crystal structures. Coating phase structure was characterized by image plate X-ray diffractometer (XRD, Italstructures, Riva del Garda, Italy) using filtered CuK_α radiation operated at 40 kV and 30 mA. The used exposure time was 2 h and the analyzed spectra taken from 2θ range of 20–120°. The incident angle (Ω) between the X-ray source and specimen surface was 15°. XRD analysis for the phosphate sealed coatings were made after grinding approximately 50 μm layer from the surface, because reaction products on the coating surface normally differ considerably from those below the surface. Structural quantitative analyses from XRD

Table 2
Laser glazing parameters and coating abbreviations

	$8Y_2O_3$–ZrO_2	$25CeO_2$–$2.5Y_2O_3$–ZrO_2	22.5MgO–ZrO_2
Coating abbreviation	8YL	25CL	22ML
Laser power (kW)	4.0	3.0	3.5
Surface speed (mm/min)	3500	4000	4500
Surface distance from the mirror (mm)	80	80	80
Laser beam specific energy density (J/mm^2)	6.9	4.5	4.7

patterns were made by the Rietveld method[34] using MAUD software (Material Analysis Using Diffraction, version 1.87 (Luca Lutterotti, University of Trento, Italy). MAUD software was used also in determining the texture of laser-glazed coatings. Total porosity was evaluated by image analysis using optical microscope (Carl Zeiss Axiophot, Germany) and image acquisition and analysis software (QWin, Leica Microsystems, Switzerland). The results and their deviations are presented as a mean value of five separate analyses from each type of coating. Open porosity was measured with mercury porosimetry (models Pascal 140 and Porosimeter 2000, CE-instruments, Milan, Italy) over the pressure range of 0.1 kPa−200 MPa.

3. Results and discussion

3.1. As-sprayed coatings

The optical micrographs of the as-sprayed coatings are presented in Fig. 1. In all coatings the typical microstructure of the plasma sprayed TBCs can be seen with pores, lamellae boundaries and microcracks. Total porosity of the coatings was evaluated by image analysis from the polished coating cross sections and the values were in the range of 12.1–20.7%. The open porosities, measured by mercury porosimetry, varied between 9.3 and 10.4%. The pore size distribution of open porosity varied in the range of 0.006–10 μm, and the major fraction of the pores was found at 0.1–0.5 μm. The results of total porosity determination by image analysis were very sensitive to the specimen preparation. Usually the evaluated total porosity values are too high because in specimen preparation procedure some defects, namely pull-outs, can be introduced and identified as pores. So for that reason the real total porosity could be expected to be something between the evaluated total porosity and measured open porosity. The Vickers $HV_{0.3}$ microhardnesses varied from 607 of the 22M coating up to 713 of the 8Y coating. The porosity and microhardness values of the as-sprayed coatings are presented in Table 3.

The results of the quantitative XRD phase structure analysis for the powders and as-sprayed coatings are presented in Table 4. The $8Y_2O_3$–ZrO_2 powder (Metco 204 NS) consisted mostly of the nontransformable tetragonal zirconia (t′-ZrO_2), but monoclinic zirconia (m–ZrO_2) was also detected. XRD analysis did not show the presence of the cubic zirconia (c-ZrO_2). However, Ilavsky et al. [35] showed by neutron diffraction analysis that in the equivalent $8Y_2O_3$–ZrO_2 HOSP powder there was a notable fraction of c-ZrO_2. By neutron diffraction they obtained the data from the total volume of the powder while our results are mainly from the surface of the individual powder particles. The properties of the

Table 3
Microhardness and porosity results of the as-sprayed coatings

Coating	Microhardness $HV_{0.3}$	Total porosity (%) (image analysis)	Open porosity (%) (mercury porosimetry)
8Y	713	20.7±1.8	9.3±1.0
25C	689	18.4±3.3	10.4±1.0
22M	607	12.1±2.2	9.5±1.0

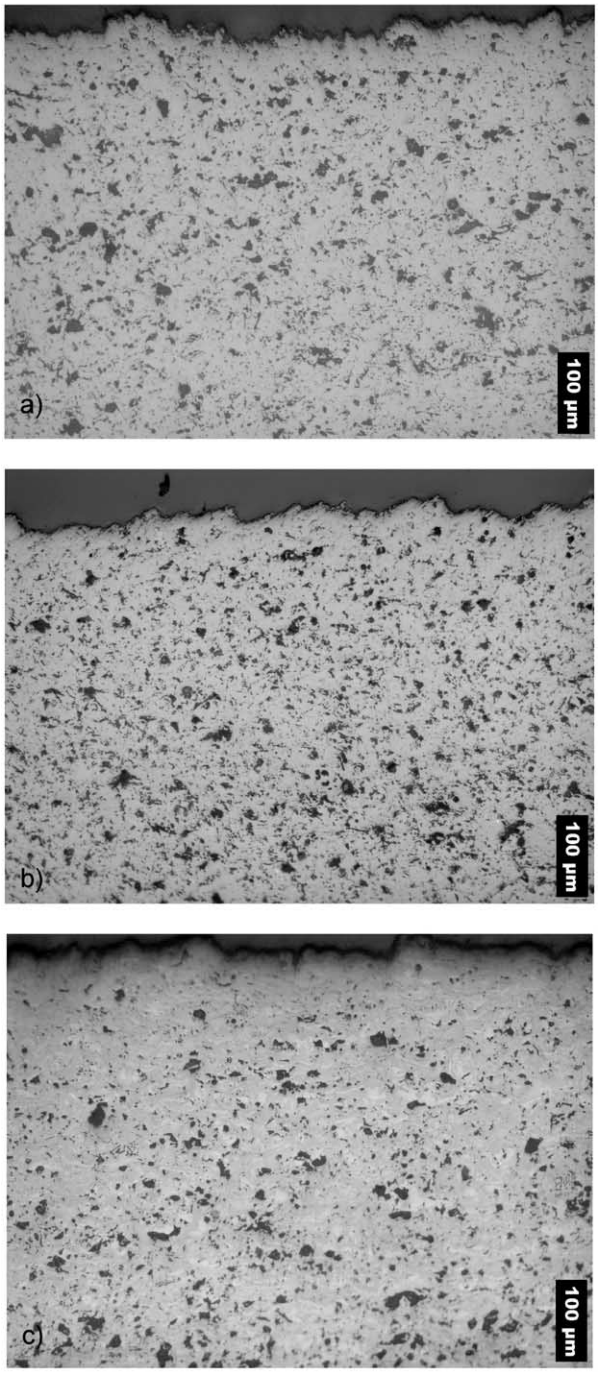

Fig. 1. Optical micrographs of the as-sprayed coatings: (a) 8Y, (b) 25C and (c) 22M.

surface and core of the HOSP powder differ a lot due to the plasma densification process of the particles. So for that reason the difference of the results can be explained by the different penetration depth of the neutrons and X-rays, and also by the nature of the HOSP powder.

After plasma spraying the 8Y structure was stabilized almost completely and only a minor amount of m-ZrO_2 was identified. The small fraction of m-ZrO_2 originates likely from the unmelted portion of the feedstock powder. The major stabilized phase was t′-ZrO_2, in addition to some per cents of c-ZrO_2. The phase structure of the 25CeO_2–2.5Y_2O_3–ZrO_2 powder (Metco 205 NS) was more complex and was composed nearly equal parts of m-ZrO_2, t′-ZrO_2 and c-ZrO_2. A small amount of cubic cerianite (c-CeO_2) was also detected. The small amount of cerianite was also identified from the as-sprayed 25C coating together with stabilized zirconia phases t′-ZrO_2 and c-ZrO_2. In SEM studies, the free c-CeO_2 was detected by EDS point analysis and seen randomly in backscattered electron images as lighter lamellae. The 22MgO–ZrO_2 spray powder (ZRO-103) consisted of c-ZrO_2 and cubic magnesia (c-MgO, periclase structure) phases. After plasma spraying there still was a notable volume fraction, 26%, of free MgO in structure, in addition to c-ZrO_2 and t′ZrO_2 phases. The inhomogeneity of the 22M coating microstructure were observed as a different gray levels of lamellae from optical and SEM micrographs, also seen in Fig. 1c.

3.2. Laser-glazed coatings

The optical micrographs of the laser-glazed coatings are presented in Fig. 2. Laser-glazed coatings were highly densified within the melted surface layer, with the exception of some closed pores and vertical cracks that were formed in glazing process. The thickness of the melted zone varied locally between 50 and 150 μm and depended on the coating material. Two types of vertical cracks were detected from the all laser-glazed coatings. Within the melted layer there were some microcracks, with length shorter than the layer thickness. There were also some longer macrocracks, 200–500 μm in length, which went through the glazed layer and further. In 8YL coating the macrocracks were rather straight lined in vertical direction. Instead of that some of the macrocracks in 25CL coating were branched out below the melted layer and shifted from the vertical direction. In 22ML coatings the vertical cracks were more irregular and in some cases they coalesced below the melted layer and caused partial peeling of the glazed zone. The straight vertically lined cracks could be more preferential if the strain tolerance properties of the coating are considered. All the macrocracks in the laser-glazed coatings were counted from the specimen cross sections and macrocrack density is presented in Table 5.

Total porosity values of the laser-glazed layers varied in 2.8–4.9%, when not taking into account the macrocracks. Most of the pores were spherical and located at the lower region of the melted layer. The rest of the porosity was in the form of vertical microcracks. Reliable mercury porosimetry could not be applied to the laser-glazed coatings, because it was impossible to prepare proper specimens of the melted top layers. And if it was measured over the total coating thickness, the interpretation of the results was impossible.

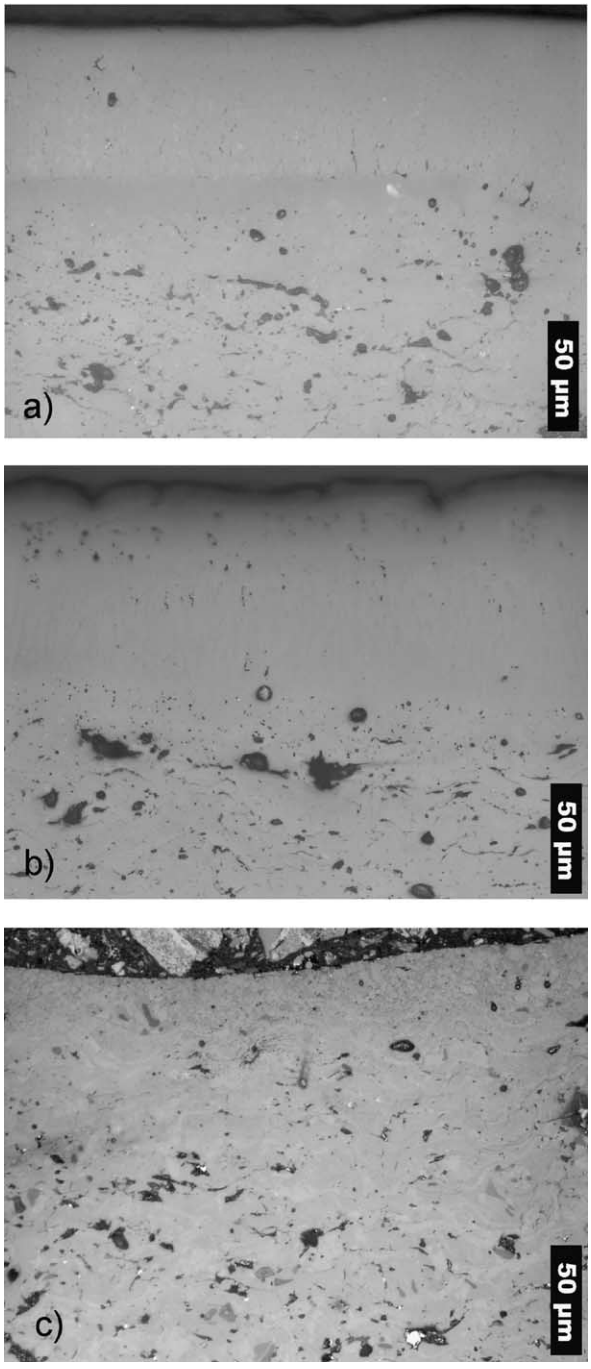

Fig. 2. Optical micrographs of the laser-glazed coatings: (a) 8YL, (b) 25CL and (c) 22ML.

Table 4
The phase composition of the as-sprayed coatings and powders

Coating/powder	m-ZrO_2 (vol.%)	t′-ZrO_2 (vol.%)	c-ZrO_2 (vol.%)	Other phases (vol.%)
8Y powder Metco 204 NS	20	80	–	–
8Y	3	92	5	–
25C powder Metco 205 NS	29	36	31	CeO_2 = 4
25C	–	72	25	CeO_2 = 3
22M powder ZRO-103	–	–	65	MgO = 35
22M	–	19	55	MgO = 26

Microhardness of the coating top layers increased from the base level of 600–700 $HV_{0.3}$ up to 1100–1250 $HV_{0.3}$. The porosity and microhardness results of the laser-glazed coatings are presented in Table 5.

The optical microscopy study showed that the glazing had occurred at quite smoothly in 8YL and 25CL coatings, but in magnesia stabilized coating the thickness of the melted layer varied quite much. The high amount of free MgO in 22M coating structure had possibly caused the irregular melting of the surface. The vapor pressure of the MgO is much lower than that of ZrO_2 and for that reason the strong evaporation of MgO had probably caused some of these irregularities in melted layer. The coatings were laser-glazed in as-sprayed state and their original surface roughness (R_a) was quite equal and around 5 μm, so that did not cause the differences. 8YL coatings had transparent and glassy-like surface due to the appropriate laser beam absorption and sufficient melting. The surface topography of the 25CL coating was also rather smooth, but some craters, 200–500 μm in diameter, were opened to the surface. The craters were likely generated when the entrapped gas, from the coating porosity, was escaping from the melt pool during the glazing process. Respectively, the surface of the 22ML coating was quite coarse with lots of craters. The color of the yttria stabilized zirconia coatings changed from light grey to transparent white due to the laser glazing procedure. In our earlier study, the color of the laser-glazed $8Y_2O_3$–ZrO_2 coating was closer to transparent yellow instead of white [26] In that case the spray powder was different and the powder and coating contained more monoclinic zirconia. The color shade differences in plasma sprayed and laser-glazed coatings were due to the different stoichiometry of the coatings. This behavior was detected also with the 25C coating when the light gray color of the powder changed in plasma spraying to light green/yellow and then to black in laser-glazing. The reversibility of the color change was demonstrated with 25CL coating by performing a simple heat treatment in air at 1250 °C for 5 h, when the color was changed back close to the original color of the feedstock powder. The white color of the 22M did not change in laser treatment.

SEM studies showed the columnar/dendritic structure of the laser-glazed layers in all coatings, see Fig. 3. However, the uppermost layer of the 8YL coating was formed of pentagon and hexagon shaped plates and the underneath layer of columnar/dendritic grains; see the marked layers in Fig. 4. In some places the thickness of the plate-like layer reached 40 μm, but the plate-like structure did not cover the entire surface. Some voids could be detected at the lower region of the melted zone, marked with an arrow in Fig. 4. Large voids were probably developed with the same mechanism like the craters at the coating surface.

The quantitative XRD analysis results of the laser-glazed coatings are presented in Table 6. In the laser-glazing of the 8Y and 25C coatings the zirconia phase structure was totally stabilized to t′-ZrO_2. In both coatings the structure was identified to be pure t′-ZrO_2 with no cubic phase present. The discrete lines and spots in the image plate spectrum of the 8YL coating showed the large grain size of the plate-like surface layer. In 25CL coating there still was some free CeO_2 like there was in the spray powder and in the as-sprayed coating. The pure t′-ZrO_2 structure indicated the complete melting of the surface layer in laser-glazing process and very rapid solidification and cooling of the crystals at the surface. In the 22ML coating the rhombohedral $Mg_2Zr_5O_{12}$ was the dominating phase after the laser-glazing, but c-ZrO_2 and c-MgO were also present. No tetragonal phase was identified. EDS analysis showed approximately 8 wt.% of the MgO within the dendrite structure, and respectively 17 wt.% between the dendrites. This indicated that the dendrites were composed of $Mg_2Zr_5O_{12}$ crystals of and the rest of the structure of c-ZrO_2 and c-MgO.

Table 5
Microhardness and porosity results of the laser-glazed coatings

Coating	Thickness of the sealed layer (μm)	Macrocrack density[a] (1/mm)	Microhardness[b] $HV_{0.3}$	Total porosity[a] (%) (image analysis)
8YL	100–150	1.5	1240	2.8 ± 2.6
25CL	50–100	1.4	1189	4.9 ± 2.1
22ML	50–100	1.9	1119	3.3 ± 1.6

[a] Average value from the total cross section (ø = 25 mm) was counted visually by using optical microscope.
[b] Measured only from the melted zone.

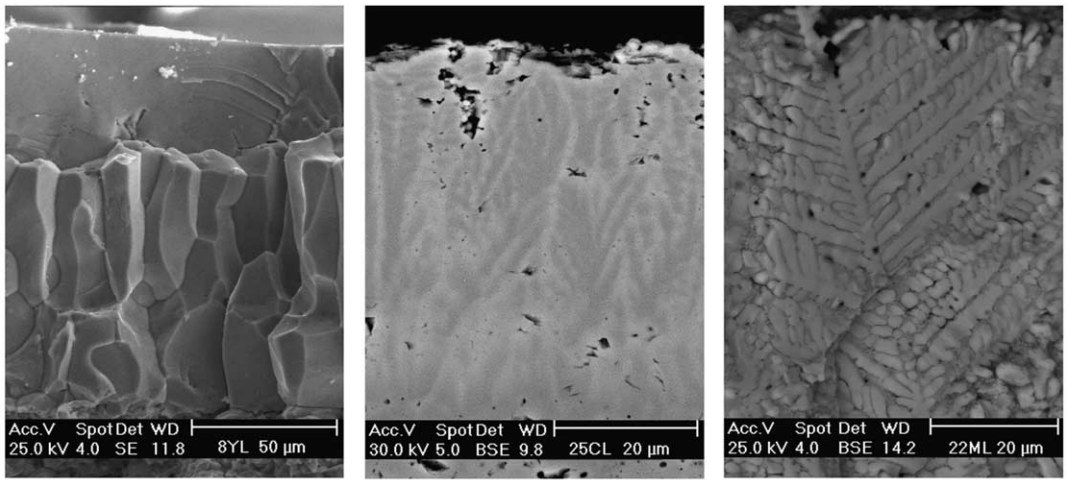

Fig. 3. Columnar and dendritic structures of the laser-glazed coatings: (a) dense plate-like top layer and vertically oriented columnar grains in the fracture surface of the 8YL coating, (b) vertically orientated grains in the polished cross section of the 25CL coating and (c) dendrite arm structure in the fracture surface of the 22ML coating.

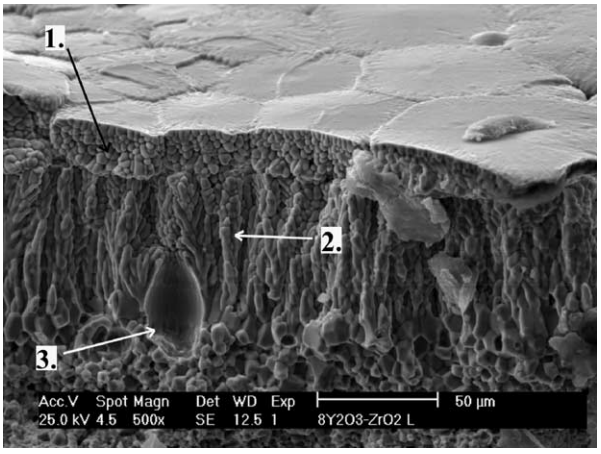

Fig. 4. The fracture surface of the 8YL coating: (1) pentagon/hexagon shaped plates in top layer (2) vertically orientated grains (3) a closed pore within the lower region of the melted layer.

The texture analysis, performed with MAUD software and using the XRD data, showed the preferred crystal orientation of the laser-glazed coatings, especially in 25CL coating. In 25CL coating the texture was very strong and the preferred orientation was determined in [002] direction. The XRD spectra of the 25C and 25CL coatings are compared in Fig. 5. The preferred crystal orientation of the t′-ZrO_2 phase in 25CL coating can be seen quite clearly as a change of the relative intensities of the diffraction peaks. Reconstructed pole figs. of the t′-ZrO_2 phase, in the 25CL coating, show also the texture principally in [002] direction, see Fig. 5b. In mrd scale the value 1 represent random powder orientation. The highest measured values for 8Y coating were below 1.5. The colors demonstrate the diffraction peak intensity and the preferred orientation can be determined by the local color changes inside the circle. The center of the circle corresponds to the surface normal direction. All the pole figures are revolution symmetric with the center which indicates of fiber texture. In the case of 8YL coating the preferred crystal orientation was not as clear as in the 25CL coating. In the plate-like top layer there was not clear preferred crystal orientation and the low penetration depth, 5–10 µm, of the CuK_α into the zirconia made it difficult to analyze the texture of the columnar grains below the coating surface. XRD measurements and texture analysis were repeated also after grinding the plate-like layer off, but due to its unequal thickness and extremely high hardness, the uniform removal was not successful. The texture analysis was difficult to perform for the 22ML coating because of the three present, partly overlapping, phases in XRD pattern. However, the typical dendrite growth directions ($Mg_2Zr_5O_{12}$ phase) in laser-glazed layer could be seen in micrographs, as in the Fig. 3c.

Table 6
The phase composition of the laser-glazed coatings

Coating	m-ZrO_2 (vol.%)	t′-ZrO_2 (vol.%)	c-ZrO_2 (vol.%)	Other phases (vol.%)
8YL	–	100	–	–
25CL	–	96	–	CeO_2 = 4
22ML	–	–	16	$Mg_2Zr_5O_{12}$ = 66, MgO = 18

3.3. Phosphate sealed coatings

Optical microscopy studies showed that the phosphate based sealants penetrated approximately 300–400 µm into the coatings, see Fig. 6. Total porosity of the phosphate sealed coatings was decreased to the level of 7.5–12.9%, depending on the coating material.

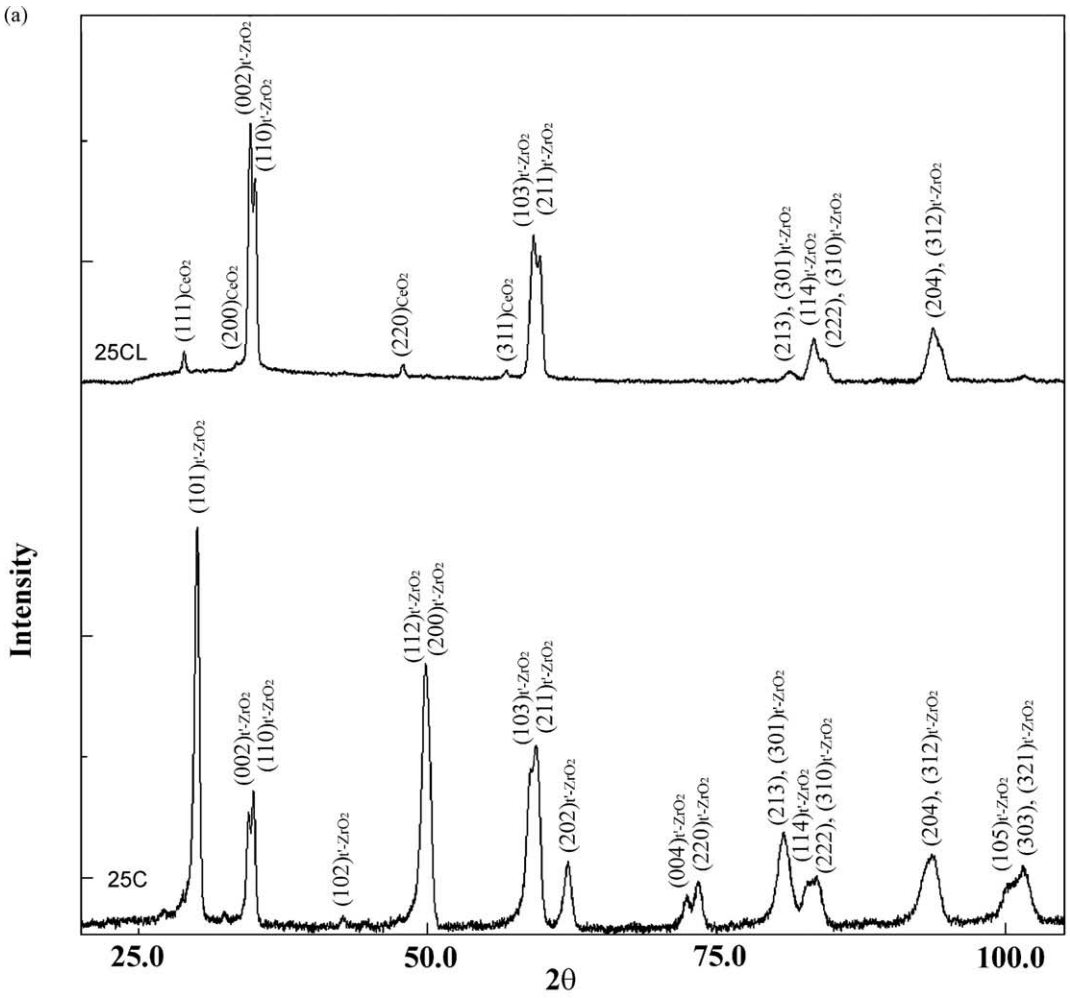

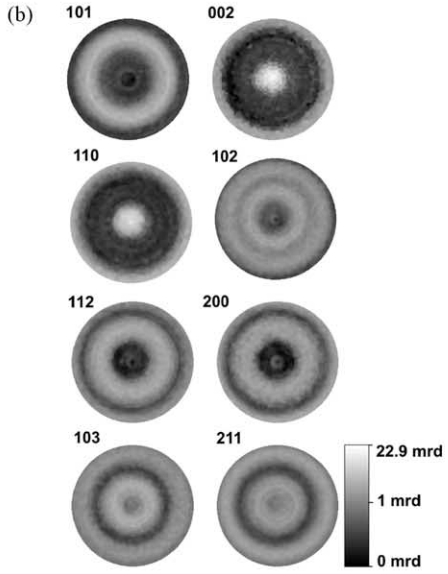

Fig. 5. XRD patterns of the 25C and 25CL coatings (b) reconstructed pole figures (log scale) of the t′-ZrO_2 phase in 25CL coating.

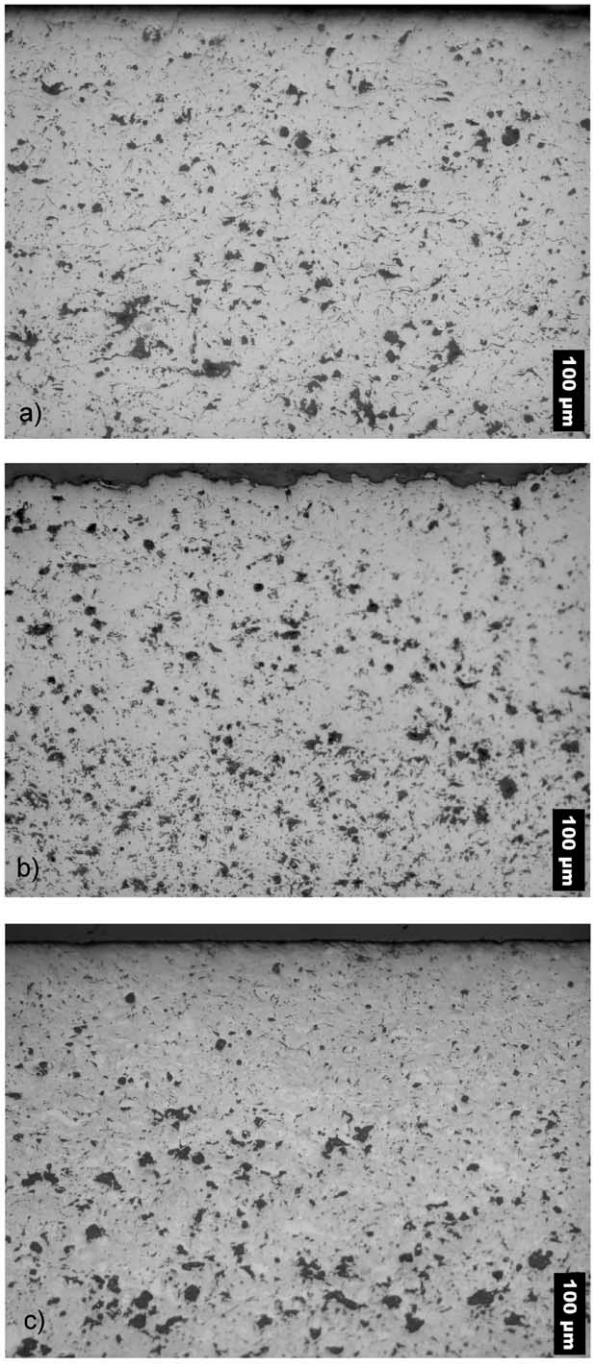

Fig. 6. Optical micrographs of the phosphate sealed coatings: (a) 8YAP, (b) 25CAP and (c) 22MOPA.

Respectively the open porosities were lowered to the level of 5.3–7.3%. So if compared the porosity results to the as-sprayed coatings the reduction in total porosities were 30–39% and in open porosities 24–48%. Mercury porosimetry values represent the mean open porosity of the entire coating, so that the real open porosities of the sealed top layers might be even lower. Results of the porosity measurements are presented in Table 7. Due to the phosphate sealing the microhardness values increased from the base level of 600–700 $HV_{0.3}$ up to 820–880 $HV_{0.3}$, see Table 7. Approximately the same penetration depth of the sealant was confirmed in our earlier study by performing a microhardness profiles from the coating cross sections [26] The microhardness increase of the sealed coatings is probably consequence of the denser structure and better bonding of the lamellae. The higher hardness values also indicated an increased stiffness of the sealed structures. Earlier we found [25] that the aluminum phosphate sealing treatment induces compressive stresses at the surface of $8Y_2O_3$–ZrO_2 coatings. The compressive stresses are likely generated according to the following steps: the sealant is impregnated in to the coating at room temperature ⇒ the structure is heated up to 300 °C ⇒ the sealant binds the coating structure at 300 °C ⇒ the stiffness of the coating increases ⇒ after the treatment the system cools down to the room temperature ⇒ at this stage the stiffer coating structure tries to return to its original state due to the metallic substrate ⇒ compressive stresses are induced, because of the mismatch in coefficients of thermal expansion of metallic substrate and sealed ceramic coating. The stresses induced by phosphate sealing are considered more detail in Ref. 36.

TEM studies were performed for the aluminum phosphate sealed 8Y coating in order to clarify the bonding and strengthening mechanism related to the phosphate sealing. In our earlier studies [37,38] we found that depending on the coating material, the strengthening is the result of two different mechanisms, namely chemical bonding or/and adhesive binding. In the first case there is a chemical reaction and bonding with the coating material and the sealant and in the latter case the strengthening is based on formation of the condensed phosphates in the structural defects of the coating. Phosphate sealant, penetrated into the interlamellar

Table 7
Microhardness and porosity results of the phosphate sealed coatings

Coating	Thickness of the sealed layer (μm)	Microhardness[a] $HV_{0.3}$	Total porosity[a] (%) (image analysis)	Open porosity[b] (%) (mercury porosimetry)
8Y AP	300–400	825	12.6±1.9	5.3±1.0
25C AP	300–400	882	12.9±2.4	5.4±1.0
22M OPA	300–400	844	7.5±1.6	7.2±1.0

[a] From the (sealed) top layer.
[b] Mean through thickness porosity (when coatings were sealed on both sides).

crack in 8YAP coating, is presented in TEM micrograph in Fig. 7. The high magnification TEM images showed that there is no visible reaction layer in the coating/sealant interface, so we can assume that the bonding is based mainly on latter mechanism. SAED ring patterns verified the amorphous structure of the sealant, if compared to the SAED pattern taken from the coating lamella, see Fig. 8.

The quantitative XRD analyses results of the phosphate sealed coatings, after grinding off the 50 μm thick surface layer, are presented in Table 8. The sealant phases could not be identified by XRD, because of the low concentration of the bonding phases and their amorphous microstructure. But if the 22M OPA and 25C AP coatings were just slightly grinded before the XRD analysis, clear zirconium phosphate (ZrP_2O_7) peaks were identified. However, we should consider that in the coating surface the detectable reaction surface area for XRD analysis was higher and there were a lot of sealant available for the reaction. Anyway, the same reaction could be expected to taken place also in cracks and pores. So on basis of these results it is possible that the strengthening mechanism of the 22M OPA and 25C AP differs that from the 8Y AP coating.

4. Conclusion

In this paper we presented microstructural characterization results of various modified thick thermal barrier

Table 8
The phase composition of the phosphate sealed coatings

Coating	m-ZrO_2 [vol.%]	t′-ZrO_2 (vol.%)	c-ZrO_2 (vol.%)	Other phases (vol.%)
8Y AP	3	92	5	–
25C AP	–	60	39	CeO_2 = 1, traces of ZrP_2O_7[a]
22M OPA	–	19	55	MgO = 26, traces of ZrP_2O_7[a]

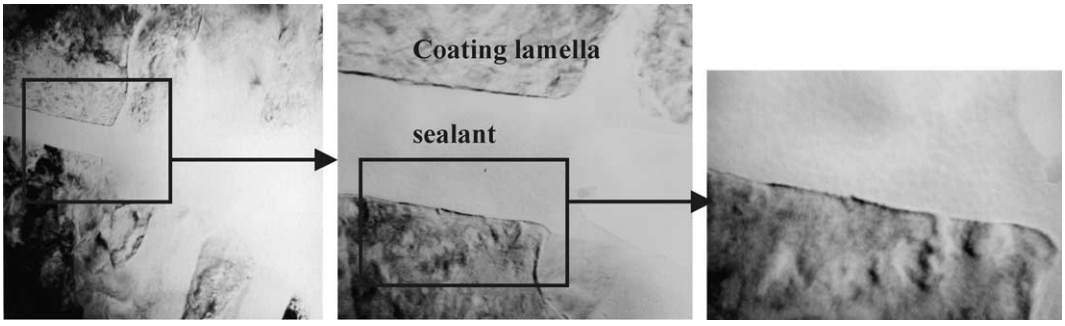

Fig. 7. TEM micrographs of interlamellar region of the 8YAP coating filled with the sealant.

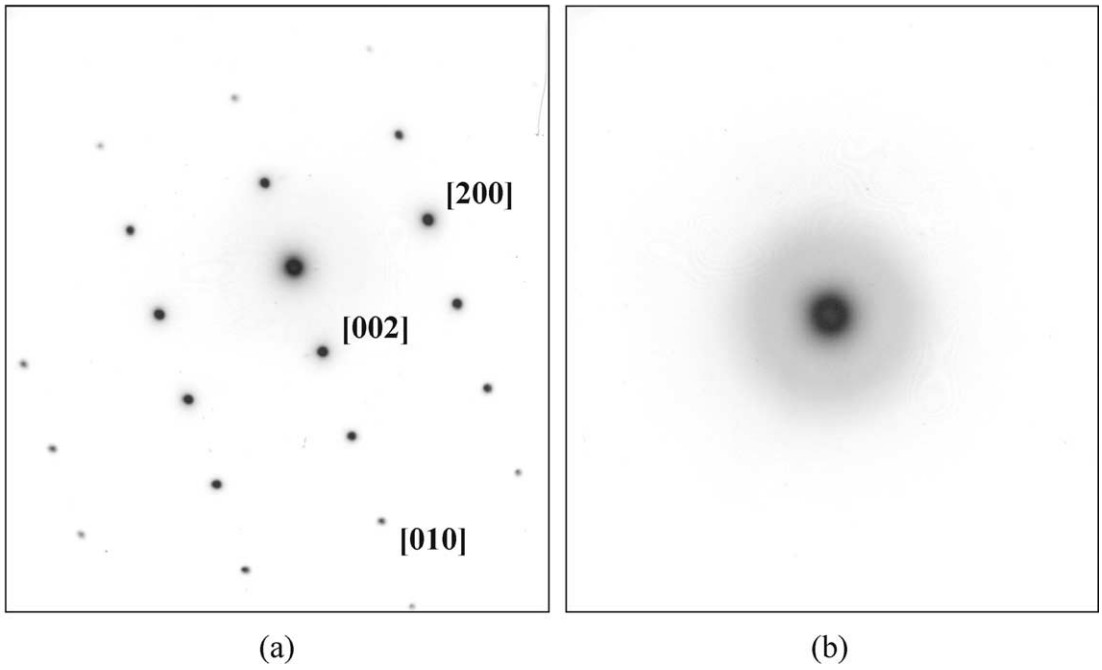

Fig. 8. SAED patterns of the 8YAP coating: (a) coating lamella and (b) sealant penetrated into the interlamellar region.

coatings. The microstructures of thick plasma sprayed $8Y_2O_3$–ZrO_2, $25CeO_2$–$2.5Y_2O_3$–ZrO_2 and 22MgO–ZrO_2 coatings were modified with laser-glazing and phosphate based sealing treatments. The main results of this study can be summarized as follows:

- The optimal thickness of the melted layer in laser glazed TTBCs was 50–150 μm. In all cases the melted zone was significantly densified and vertical macrocrack network was introduced. In the laser-glazed $8Y_2O_3$–ZrO_2 coating the vertical cracks were nearly perpendicular to the surface, but in other coatings the cracks had a tendency to branch and turn from the vertical direction below the melted layer. Due to the denser microstructure, the microhardness of surface layer in laser-glazed coatings was increased up to 1119–1240 $HV_{0.3}$. The t′-ZrO_2 was a dominating phase of the laser-glazed $8Y_2O_3$–ZrO_2 and $25CeO_2$–$2.5Y_2O_3$–ZrO_2 coatings whereas the phase structure of the magnesia stabilized zirconia changed from c-ZrO_2 + t′ZrO_2 to the mixture of rhombohedral $Mg_2Zr_5O_{12}$ and c-ZrO_2. Texture analysis showed a strong preferred crystal orientation in direction [002] of the t′-ZrO_2 phase in laser-glazed $25CeO_2$–$2.5Y_2O_3$–ZrO_2 coating.
- In phosphate sealed coatings the penetration depth of the sealant was approximately 300–400 μm and microhardness at the range of 825–882 $HV_{0.3}$. The open porosity of the phosphate sealed coatings was reduced by 24–48% depending on the coating material. Traces of the ZrP_2O_7 were identified at the surfaces of the 22M OPA and 25C AP coatings, but any crystalline phosphate phases were not detected when 50 μm thick surface layers were grinded off. However, TEM studies and EDS analysis showed the phosphate phases in coating structural defects and revealed their amorphous microstructure. Adhesive binding was defined as strengthening mechanisms of the aluminum phosphate sealed $8Y_2O_3$–ZrO_2 coating.

Acknowledgements

Results in this paper have been collected from studies carried out during the years 2001–2002 in Tampere University of Technology, Finland and University of Trento, Italy. The work was financed mainly by the Academy of Finland and the work has been partially developed within the frame of ''Ricerca di Sistema'' D.L. MICA 26/01/2000. In addition to the financial supporter, the authors are grateful to Mr. Jari Tuominen and Mr. Mikko Kylmälahti for assistance in preparing the coating specimens.

References

1. Assanis, D. N., Thin thermal barrier coatings for internal combustion engine components. *Int. J. Mater. Prod. Technol.*, 1989, **4**, 232–243.
2. Kvernes, I., Potential of coatings in diesel engines. In *High Temperature Materials for Power Engineering 1990 Proceedings*, ed. R. Bachelet, R. Brunetaud, D. Coutsouradis, P. Esslinger, J. Ewald, I. Kvernes, Y. Lindblom, D. B. Meadowcroft, V. Regis, R. B. Scarlin, K. Schneider and R. Singer. Kluwer Academic Publishers, Dordrecht, The Netherlands, 1990, pp. 843–864.
3. Yonushonis, T. M., Overview of thermal barrier coatings in diesel engines. *J. Therm. Spray Techn.*, 1997, **6**(1), 50–56.
4. Beardsley, M. B., Thick thermal barrier coatings for diesel engines. *J. Therm. Spray Techn.*, 1997, **6**(2), 181–186.
5. Brink, R. C., Material property evaluation of thick thermal barrier coating systems. *Trans. ASME*, 1989, **111**, 570–577.
6. Novak, R. C., Matarese, A. P., Huston, R. P., Scharman, A. J. and Yonushonis, T. M., Development of thick thermal barrier coatings for diesel applications. *Materials and Manufacturing Processes*, 1992, **7**(1), 15–30.
7. Osawa, K., Kamo, R. and Valdmanis, E., Performance of thin thermal barrier coating on small aluminium block diesel engine. *SAE Technical Paper Series*, 1991, **910461**, 1–8.
8. Singh, J. P., Nair, B. G., Renusch, D. P., Sutaria, M. P. and Grimsditch, M. H., Damage evolution and stress analysis in zirconia thermal barrier coatings during cyclic and isothermal oxidation. *J. Am. Ceram. Soc.*, 2001, **84**(10), 2385–2393.
9. Evans, A. G., Mumm, D. R., Hutchinson, J. W., Meier, G. H. and Pettit, F. S., Mechanisms controlling the durability of thermal barrier coatings. *Prog. Mater. Sci.*, 2001, **46**, 505–553.
10. Ilavsky, J. and Stalick, J. K., Phase Composition and its changes during annealing of plasma-sprayed YSZ. *Surf. Coat. Tech.*, 2000, **127**, 120–129.
11. Zhu, D. and Miller, R. A., Thermal conductivity and elastic modulus evolution of thermal barrier coatings under high heat flux conditions. *J. Therm. Spray Techn.*, 2000, **9**(2), 175–180.
12. Ohmori, A., Zhou, Z., Inoue, K., Murakami, K. and Sasaki, T., Sealing and strengthening of plasma-sprayed ZrO_2 coating by liquid Mn alloy penetration treatment. In *Thermal Spraying: Current Status and Future Trends*, ed. A. Ohmori. High Temperature Society of Japan, Osaka University, Osaka 567, Japan, 1995, pp. 549–554.
13. Zaplatynsky, I., Performance of laser-glazed zirconia thermal barrier coatings in cyclic oxidation and corrosion burner rig test. *Thin Solid Films*, 1982, **95**, 275–284.
14. Sivakumar, R. and Mordike, B. L., Laser melting of plasma sprayed ceramic coatings. *Surface Engineering*, 1988, **4**(2), 127–140.
15. Jasim, K. M., West, D. R. F., Steen, W. M. and Rawlings, R. D., Laser surface sealing of plasma sprayed yttria stabilized zirconia ceramics. In *Proceedings of the Laser Materials Processing 1988*, Springer-Verlag, Heidelberger, Berlin, 1989, pp. 17–31.
16. Tsai, H. L. and Tsai, P. C., Microstructures and properties of laser-glazed plasma-sprayed ZrO_2-YO_{15}/Ni-22Cr-10Al-1Y thermal barrier coatings. *J. Mater. Eng. Perform.*, 1995, **4**(6), 689–696.
17. Khor, K. A. and Tana, S., Pulsed laser processing of plasma sprayed thermal barrier coatings. *J. Mater. Process. Tech.*, 1997, **66**, 4–8.
18. Zhou, Z., Eguchi, N., Shirasawa, H. and Ohmori, A., Microstructure and characterization of zirconia-yttria coatings formed in laser and hybrid spray process. *J. Therm. Spray Techn.*, 1999, **8**(3), 405–413.
19. Ferriere, A., Lestrade, L., Rouanet, A., Denoirjean, A., Grimaud, A. and Fauchais, P., Solar furnace surface treatment of plasma-sprayed thermal barrier coatings. *J. Therm. Spray Techn.*, 1994, **3**(4), 362–370.

20. Kuribayashi, H., Suganuma, K., Miyamoto, Y. and Koizumi, M., Effect of HIP treatment on plasma-sprayed ceramic coating onto stainless steel. *Am. Ceram. Soc. Bull.*, 1986, **65**(9), 1306–1310.
21. Khor, K. A. and Loh, N. L., Hot isostatic pressing of plasma sprayed thermal barrier coating systems. *Materials and Manufacturing Processes*, 1995, **10**(6), 1241–1256.
22. Moriya, K., Zhao, W. and Ohmori, A., Improvement of plasma-sprayed ceramic coatings treated by sol-gel process. In *Thermal Spraying: Current Status and Future Trends*, ed. A. Ohmori. High Temperature Society of Japan, Osaka University, Osaka 567, Japan, 1995, pp. 1017–1021.
23. John, G. and Troczynski, T., Surface modification of thermal sprayed coatings. In *Thermal Spray: Practical Solutions for Engineering Problems*, ed. C. C. Berndt. ASM International, Materials Park, OH-USA, 1996, pp. 483–488.
24. Troczynski, T., Yang, Q. and John, G., Post-deposition treatment of zirconia thermal barrier coatings using sol-gel alumina. *J. Therm. Spray Techn.*, 1999, **8**(2), 229–234.
25. Ahmaniemi, S., Vuoristo, P. and Mäntylä, T., Effect of aluminum phosphate sealing treatment on properties of thick thermal barrier coating. In *Thermal Spray: Surface Engineering via Applied Research*, ed. C. C. Berndt. ASM International, Materials Park, OH-USA, 2000, pp. 1087–1092.
26. Ahmaniemi, S., Vuoristo, P. and Mäntylä, T., Sealing procedures for thick thermal barrier coatings. *J. Therm. Spray Techn.*, 2002, **11**(3), 320–332.
27. Ahmaniemi, S., Tuominen, J., Vuoristo, P. and Mäntylä, T., Improved sealing treatments for thick thermal barrier coatings. *Surf. Coat. Tech.*, 2002, **151-152**, 412–417.
28. Haanappel, V. A. C., Scharenborg, J. B. A., Corbach, H. D., Fransen, T. and Gellings, P. J., Can thermal barrier coatings be sealed by metal-organic chemical vapour deposition of silica and alumina. *High Temp. Mater. Proc*, 1995, **14**(2), 57–66.
29. Knuuttila, J., Sorsa, P. and Mäntylä, T., Sealing of thermal spray coatings by impregnation. *J. Therm. Spray Techn.*, 1999, **8**(2), 249–257.
30. Schwingel, D., Taylor, R., Haubold, T., Wigren, J. and Gualco, C., Mechanical and thermophysical properties of thick pysz thermal barrier coatings: correlation with microstructure and spraying parameters. *Surf. Coat. Tech.*, 1998, **108-109**, 99–106.
31. Wigren, J., Dahlin, J. & Hansson, M. O. A Combustor Can with 1.8 mm Thick Plasma Sprayed Thermal Barrier Coating, *ASME paper 98-GT-388*, Gas Turbine & Aeroengine Congress & Exhibition, 2–5.6.1998, Stockholm, Sweden, 1998.
32. Gualco, C., Cordano, E., Fignino, F., Gambaro, C., Ahmaniemi, S., Tuurna, S., Mäntylä, T. and Vuoristo, P., An improved deposition process for very thick porous thermal barrier coatings. In *Proceedings of the International Thermal Spray Conference 2002*, ed. E. Lugscheider, DVS, Dusseldorf, Germany, 2002, pp. 196–201.
33. Steffens, H. D., Babiak, Z. and Gramlich, M., Some aspects of thick thermal barrier coating lifetime prolongation. *J. Therm. Spray Techn.*, 1999, **8**(4), 517–522.
34. Young, R. A., *The Rietveld Method*. Oxford University Press, Walton Street, Oxford, UK, 1993.
35. Ilavsky, J. and Stalick, J. K., Phase composition and its changes during annealing of plasma-sprayed YSZ. *Surf. Coat. Tech.*, 2000, **127**, 120–129.
36. Ahmaniemi, S., Vippola, M., Vuoristo, P., Mäntylä, T., Buchmann, M. and Gadow, R., Residual stresses in aluminium phosphate sealed plasma sprayed oxide coatings and their effect on abrasive wear. *Wear*, 2002, **252**, 614–623.
37. Vippola, M., Ahmaniemi, S., Keränen, J., Vuoristo, P., Lepistö, T., Mäntylä, T. and Olsson, E., Aluminum phosphate sealed alumina coating: characterization of microstructure. *Mat. Sci. Eng. A-Struct.*, 2002, **323**, 1–8.
38. Vippola, M., Ahmaniemi, S., Vuoristo, P., Lepistö, T., Mäntylä, T. and Olsson, E., Microstructural study of aluminum phosphate sealed plasma-sprayed chromium oxide coating. *J. Therm. Spray Techn.*, 2002, **11**(2), 253–260.